Active particles induce large shape deformations in giant lipid vesicles

https://doi.org/10.1038/s41586-020-2730-x

Received: 4 November 2019

Accepted: 24 July 2020

Published online: 30 September 2020

Check for updates

Hanumantha Rao Vutukuri[1,3]✉, Masoud Hoore[2,3], Clara Abaurrea-Velasco[2], Lennard van Buren[1], Alessandro Dutto[1], Thorsten Auth[2], Dmitry A. Fedosov[2], Gerhard Gompper[2]✉ & Jan Vermant[1]

Biological cells generate intricate structures by sculpting their membrane from within to actively sense and respond to external stimuli or to explore their environment[1–4]. Several pathogenic bacteria also provide examples of how localized forces strongly deform cell membranes from inside, leading to the invasion of neighbouring healthy mammalian cells[5]. Giant unilamellar vesicles have been successfully used as a minimal model system with which to mimic biological cells[6–11], but the realization of a minimal system with localized active internal forces that can strongly deform lipid membranes from within and lead to dramatic shape changes remains challenging. Here we present a combined experimental and simulation study that demonstrates how self-propelled particles enclosed in giant unilamellar vesicles can induce a plethora of non-equilibrium shapes and active membrane fluctuations. Using confocal microscopy, in the experiments we explore the membrane response to local forces exerted by self-phoretic Janus microswimmers. To quantify dynamic membrane changes, we perform Langevin dynamics simulations of active Brownian particles enclosed in thin membrane shells modelled by dynamically triangulated surfaces. The most pronounced shape changes are observed at low and moderate particle loadings, with the formation of tether-like protrusions and highly branched, dendritic structures, whereas at high volume fractions globally deformed vesicle shapes are observed. The resulting state diagram predicts the conditions under which local internal forces generate various membrane shapes. A controlled realization of such distorted vesicle morphologies could improve the design of artificial systems such as small-scale soft robots and synthetic cells.

Active or self-propelled particles (SPPs) have been shown to accumulate at hard surfaces[12] and in regions with high concave curvature[13] so that their activity leads to different spatial distributions compared to passive Brownian systems[14,15]. Giant unilamellar vesicles (GUVs) and biological cells represent soft confinements in which localized forces can deform the boundaries[6–8,10,11]. This may create a complex feedback loop between curvature-induced SPP accumulation, active force (swim pressure) generation and subsequent dynamic changes of vesicle shape. The possible occurrence of such a feedback loop raises questions about stationary and dynamic shapes, their transformation, activity and dependence on the number of SPPs. Simulation studies have predicted predominantly global vesicle shape changes, such as prolate vesicles with accumulation of SPPs at the poles[16,17] in two dimensions, and prolate, oblate and stomatocyte shapes[18] for floppy vesicles in three dimensions.

Here we realize and systematically characterize active vesicles by varying the number of SPPs (in experiments and simulations) and their propulsion strength (in simulations) for two different vesicle tensions. Our combined experimental and simulation study demonstrates the emergence of strongly deformed non-equilibrium shapes such as highly branched dendritic structures.

Activity-induced vesicle shapes

Self-propelled Janus colloids (half Pt-coated polystyrene) of diameter $\sigma = 1.0\,\mu m$, which have no specific interactions with the membrane (both in the absence and presence of propulsion; Extended Data Fig. 1), are encapsulated in GUVs of 1,2-dioleoyl-*sn*-glycero-3-phosphocholine lipids (Methods). These SPPs are force- and torque-free[14,15] and propel owing to diffusiophoretic forces with a velocity of v_p, controlled by varying the fuel concentration of hydrogen peroxide (H_2O_2) (Supplementary Information). When an SPP reaches the vesicle surface, it pushes against the membrane (Supplementary Video 1), and the response of the membrane opposes the propulsion force. This force is exerted on the membrane as long as the Janus particle does not reorient, which is characterized by its rotational diffusion time τ_r. The resulting

[1]Soft Materials, Department of Materials, ETH Zürich, Zürich, Switzerland. [2]Theoretical Physics of Living Matter, Institute of Biological Information Processing and Institute for Advanced Simulation, Forschungszentrum Jülich, Jülich, Germany. [3]These authors contributed equally: Hanumantha Rao Vutukuri, Masoud Hoore. ✉e-mail: h.r.vutukuri@mat.ethz.ch; g.gompper@fz-juelich.de

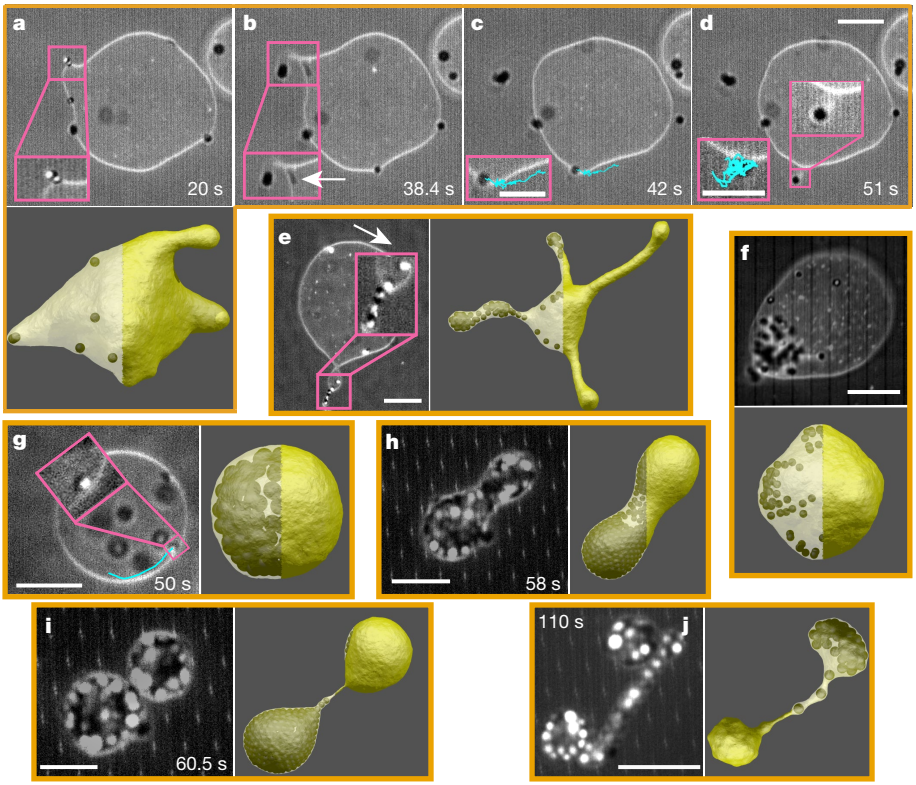

Fig. 1 | Dynamic response of the lipid membrane at a low (flaccid) and high tension of vesicles to the encapsulated SPPs at different volume fractions ϕ. **a**–**d**, Sequence of time-lapse two-dimensional confocal and bright-field microscopy images showing various membrane deformations from partial and full wrapping to tethering. **a**, Tether formation. **b**, The inset shows that a second particle enters an already existing tether. **c**–**d**, Other SPPs with partially and fully wrapped states, and subsequent budding (inset in **d**). The magenta boxes depict magnified views of particles that are either outside or in close proximity to the membrane. **e**, Tethers consisting of multiple active particles. The inset illustrates a cooperative chain-like packing of SPPs. **f**, Membrane curvature-mediated accumulation of SPPs. **g**, Dynamics of active particles in a high-tension vesicle, showing no tethering and the circular trajectory of an SPP near the membrane. **h**–**j**, Time-lapse images illustrating the shape change from a sphere to two twin vesicles connected by a tether. **a**, **e**–**j**, Simulation snapshots corroborating the experimental observations. We note that the degree of transparency of vesicle colour is varied to better visualize the SPPs inside GUVs. All scale bars are 10 μm.

membrane deformation, the elastic restoring force and the emerging complex and dynamic vesicle shapes are controlled by the SPP propulsion velocity v_p, the number N_p of SPPs, the membrane bending rigidity κ_c and the total tension $\lambda = \lambda_p + \lambda_a$, which consists of the passive tension λ_p and the active tension λ_a induced by SPPs. Three dimensionless numbers describe the importance of these parameters: the Péclet number $\mathrm{Pe} = v_p\sigma/D_t$ (D_t is the translational diffusion coefficient), which indirectly measures the propulsion force, the SPP volume fraction ϕ and the reduced tension $\lambda^* = \lambda R^2/(k_BT)$, where R is the vesicle radius, T is the temperature and k_B is the Boltzmann constant.

To elucidate the physical mechanisms involved in the formation of complex non-equilibrium vesicle structures, mesoscopic simulations are performed. The in silico model consists of active Brownian particles enclosed by a dynamically triangulated membrane[19]. Bending elasticity, membrane fluidity and area conservation are taken into account, in some cases in combination with a volume constraint for the vesicle (Methods).

A series of experiments and simulations were performed to interrogate membrane dynamics and shape transitions for two different values of the passive membrane tension λ_p and various particle concentrations ϕ. In the experiments, because the density of the internal fluid is higher than that of the external fluid, the vesicles sediment to the bottom of the observation chamber, where they flatten and can easily be imaged by combined high-speed confocal and bright-field microscopy. Figure 1a–d shows time-lapse images of the dynamic response of a vesicle to the active particles at a low particle concentration ($\phi \approx 4\times10^{-4}$) and low tension ($\lambda_p = 13 \pm 7\ \mathrm{nN\,m^{-1}}$; all uncertainties indicate mean ± s.d.). The bending rigidity ($\kappa_c = (18 \pm 6)k_BT$) and passive tension of vesicles are estimated by the analysis of the membrane undulation modes[6,20] (Methods). Even though the propulsion forces $f_p \approx 0.1$ pN (for $v_p = 15.0 \pm 2.0\ \mu\mathrm{m\,s^{-1}}$, Pe = 33–39) of a single SPP are small, for low-tension vesicles these forces are sufficient to locally deform the membrane. Tether formation is typically initiated cooperatively (inset of Fig. 1a): as a few SPPs deform the membrane (Fig. 1b), additional SPPs can become trapped in this region of higher curvature, thereby increasing the local force on the membrane and forming a tether (Supplementary Video 1). A high degree of wrapping of SPPs by the membrane slows down particle movement considerably, as shown by the overlaid particle trajectories in the insets of Fig. 1c, d, because of membrane viscoelastic resistance and the reduction of SPP accessibility to the fuel. By contrast, for high membrane tension ($\lambda_p = 25 \pm 9\ \mu\mathrm{N\,m^{-1}}$), the same propulsion force is too weak to overcome the deformation energy cost for tether formation, as shown in Fig. 1g. In this case, the SPPs follow the membrane curvature and perform a circling motion (Supplementary Video 1) similar to that of rodents in a hamster wheel.

Further, in low-tension vesicles, increase in particle concentration ($\phi \approx 3\times10^{-3}$) leads to the formation of long tubular protrusions in which SPPs become tightly packed, as illustrated in Fig. 1e. The particles that are close to the neck of a tube can change their propulsion direction via rotational diffusion and move in or out of the protrusion (inset of Fig. 1e, Extended Data Fig. 2a–d). Moreover, changes in local membrane curvature induce pronounced clustering of SPPs and lead to a cooperative wrapping process. For example, a cluster of several particles (ten) generates increased local stress, so that very long tethers

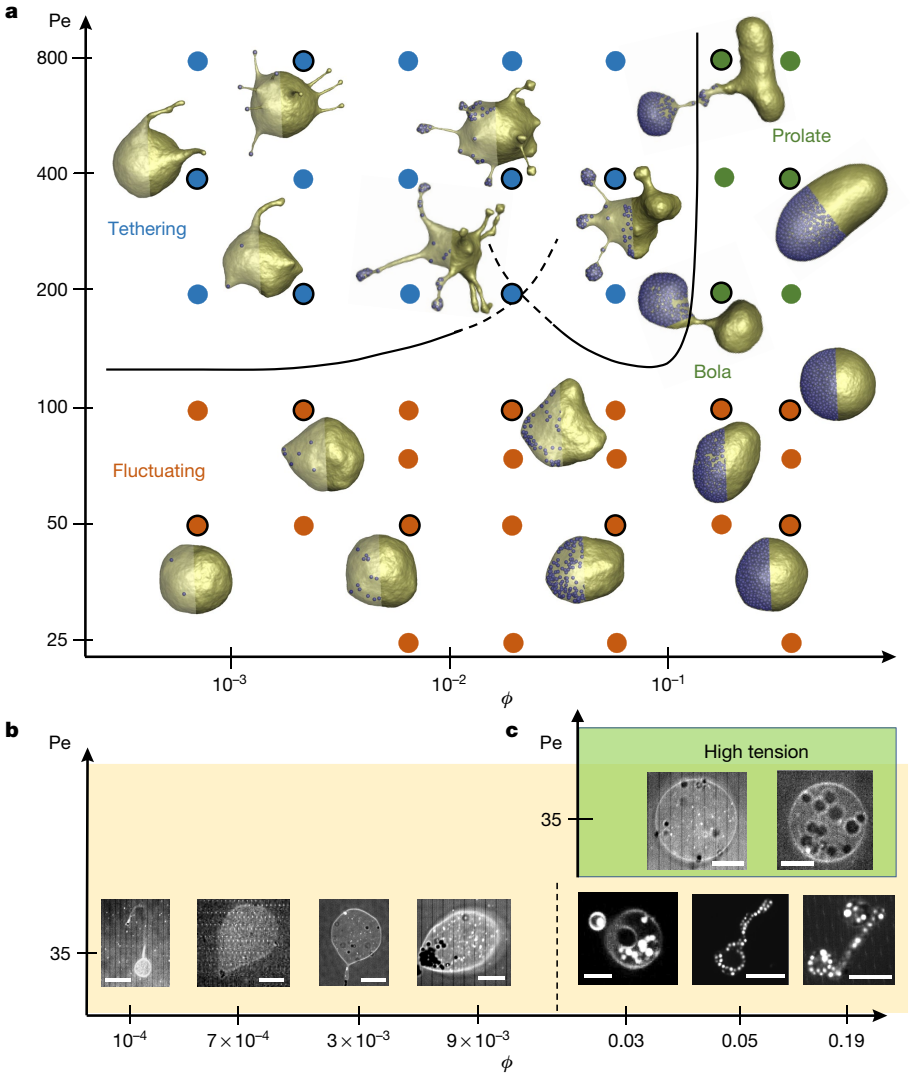

Fig. 2 | State diagram of various membrane structures. a, Simulated diagram for different Pe and ϕ values in the three regimes: tethering (blue symbols), fluctuating (red symbols) and bola/prolate (green symbols) vesicle shapes. The points corresponding to the snapshots have black outlines. All simulations are without a volume constraint and with a passive tension of $\lambda_p \approx 2\times10^{-8}$ N m^{-1}, mimicking a flaccid vesicle. The black lines correspond to theoretical estimates of the tethering boundaries with $\gamma = 0.25$ and $c_0 = 0$ (see Methods). At low ϕ, $\langle N_{p,c}\rangle = 1$, $\beta = 1$ and $\sigma_{cl} = \sigma$ are used, whereas at large ϕ, $\beta = 0.54$ and $\langle N_{p,c}\rangle$ are computed directly from simulations (Extended Data Fig. 4). **b**, The experimental shape diagram summarizes the observed vesicle shapes induced by the activity of SPPs for different ϕ and fixed Pe. **c**, High-tension vesicles are not showing any noticeable deformations. All scale bars are 10 µm.

(≈200 µm) form and remain stable until the particles reorient and the tether retracts (Extended Data Figs. 2e-j).

For SPP concentrations of $\phi \approx 10^{-2}$, many SPPs accumulate in regions of higher membrane curvature for near-spherical shapes, thereby inducing pronounced global membrane deformations; see Fig. 1f. There are two possible explanations for tether suppression and the preference for global shape changes: (i) the net propulsion force of individual particles decreases because of crowding and of their tendency to cluster owing to diffusiophoretic attraction[14,15] and (ii) activity-induced membrane tension prevents local deformations of the vesicle (see sections 'State diagram of active-vesicle shapes' and 'Shape fluctuations'). At high SPP concentrations (for example, $\phi \approx 1.9\times10^{-1}$), the vesicle can transform into bola-like and prolate shapes (Fig. 1h, i, Supplementary Video 2), with satellites connected by thin particle-laden tethers (Fig. 1j). The selected snapshots in Fig. 1, which show tethers (Fig. 1b), dendrites (Fig. 1e) and bolas and dumbbells, reveal the excellent correspondence between experiments and simulations. Supplementary Videos 3–5 demonstrate the dynamic formation of a few vesicle shapes for different Pe and ϕ values.

State diagram of active-vesicle shapes

The main focus of our simulations is the investigation of the effect of propulsion strength on the vesicle shape, and the construction of a state diagram for flaccid active vesicles (passive tension of $\lambda_p \approx 2\times10^{-8}$ N m^{-1}), where properties are predominantly determined by bending elasticity. The full state diagram as a function of Pe and volume fraction ϕ is shown in Fig. 2a for a vesicle that can freely adjust its internal volume at a fixed membrane area. The shape diagram from simulations with a volume constraint for a reduced volume of $v = 0.8$ is qualitatively similar; see Extended Data Fig. 3. Three distinct regimes are identified. (i) The 'tethering' regime, with long and thin tethers originating from a mother vesicle, occurs for large enough Pe and small-to-moderate ϕ. With increasing ϕ, the number of tethers first increases, as each SPP pulls its own tether, and then decreases, as several SPPs tend to cluster in one tether. Here, an interesting feature is the filling of the tethers by additional SPPs and the formation of large SPP clusters in small satellite vesicles at the end of the tethers. (ii) The 'fluctuating' regime for sufficiently small Pe is characterized by quasi-spherical vesicle shapes and

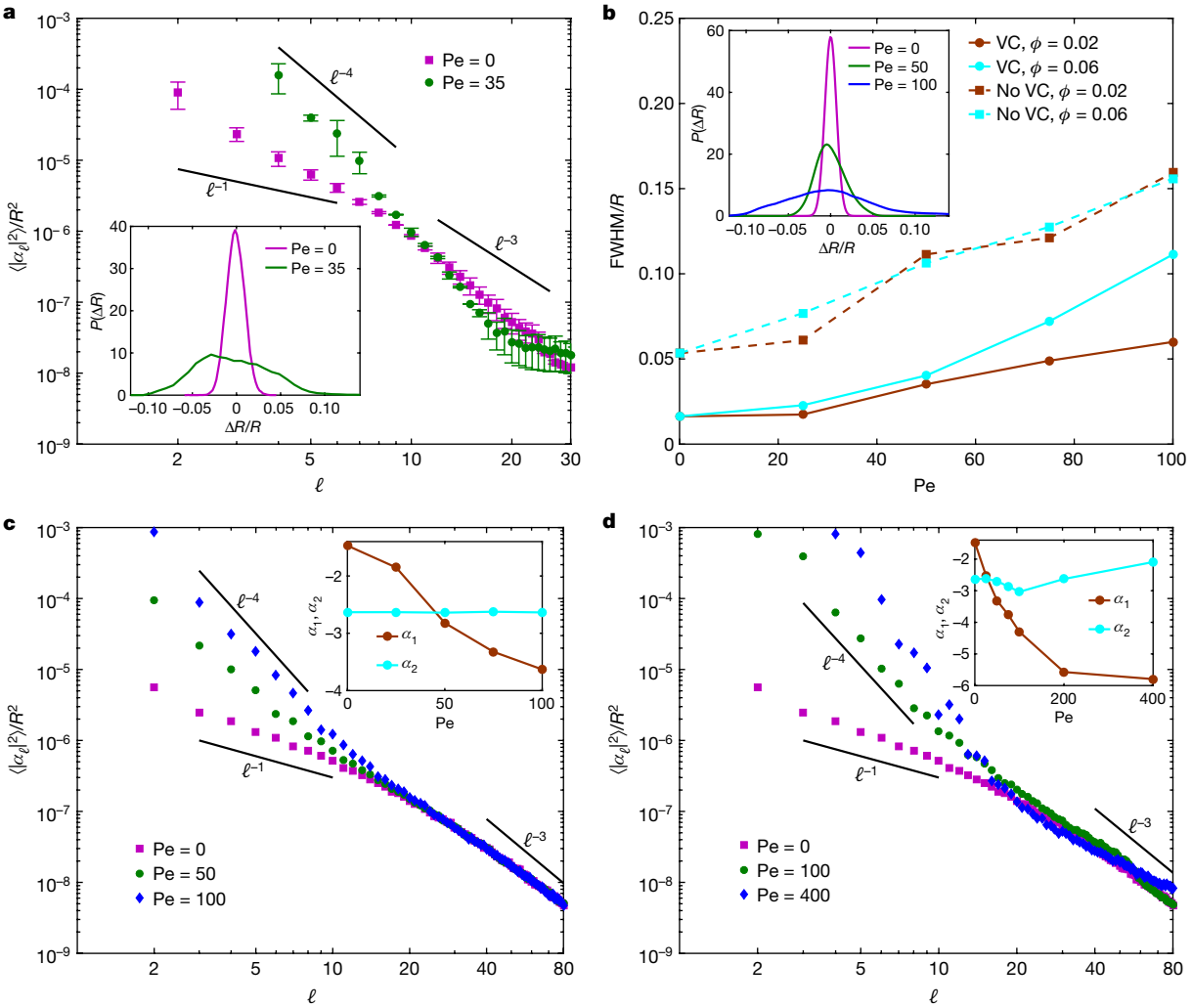

Fig. 3 | Shape fluctuation spectra for both passive and active vesicles. **a**, Experimental shape fluctuation spectra as a function of mode number ℓ for GUVs that enclose passive and active colloids with volume fraction $\phi \approx 0.009$. Inset, experimental PDFs of the radial position of the fluctuating contour from its average position for low-tension passive and active vesicles. Error bars indicate the mean ± s.d. of three independent measurements. **b**, Normalized FWHM of $P(\Delta R)$ for different Pe and ϕ with and without volume constraint (VC) from three-dimensional simulations. Inset, PDFs of the radial position of the fluctuating contour from its average position for the case with volume constraint ($0.96 < v < 0.99$) and $\phi = 0.06$. **c**–**d**, Simulation spectra for vesicles with volume constraint ($0.96 < v < 0.99$) for volume fractions $\phi = 0.06$ (**c**) and $\phi = 0.36$ (**d**) and various Pe values. The tension of the passive vesicle is found to be $\lambda_p \approx 6 \times 10^{-7}$ N m^{-1}. The insets show the exponents obtained from power-law fits to ℓ^α, measured in the ranges $3 \le \ell \le 12$ for α_1 and $35 \le \ell \le 80$ for α_2.

the absence of tethers. (iii) The 'bola/prolate' regime occurs for large Pe and ϕ and displays strong global shape changes, with the formation of two or more satellite vesicles.

The phase boundary between tethered and non-tethered vesicle shapes in Fig. 2a can be understood theoretically from the balance between the pushing forces of particle clusters, membrane curvature elasticity, and passive and active membrane tension (Methods). To pull a tether[21,22], the force $f_{p,c} = \beta N_{p,c} f_p$ of a cluster of $N_{p,c}$ SPPs with diameter $\sigma_{cl} \approx \sigma \langle N_{p,c} \rangle^{1/3}$ (where $\beta \le 1$ is the cluster cooperativity coefficient, which measures orientation alignment) must overcome the elastic membrane force $f_{tether} = \pi\sigma_{cl}(\lambda_p + \lambda_a + 2\kappa_c/\sigma_{cl}^2 - 4\kappa_c c_0/\sigma_{cl})$. For a single SPP ($N_p = 1$), this estimate yields $Pe_c \approx 140$ (for $\kappa_c = 20 k_B T$, $\lambda_p = 0$ and spontaneous curvature $c_0 = 0$), in good agreement with the simulated phase boundary in Fig. 2a for small ϕ. Higher particle loadings induce two effects: (i) the formation of oriented particle clusters with average size $\langle N_{p,c} \rangle = \alpha N_p$ that increases linearly with N_p (or equivalently ϕ), where α is a monotonically increasing function of Pe (see Extended Data Fig. 4) and (ii) an active tension due to the internal swim pressure[23], approximated as $\lambda_a = \gamma N_p f_p/(8\pi R)$ via the Young–Laplace equation ($\gamma < 1$ is the active-tension weight, as not all SPPs exert a force perpendicular to the membrane). For $\lambda_p \approx 0$, this implies that the bending rigidity term in f_{tether} decreases as $N_p^{-1/3}$, whereas the active-tension term increases as $N_p^{4/3}$. Therefore, Pe_c for tether formation first decreases at moderate ϕ owing to SPP clustering, and then increases at large ϕ because of the increasing λ_a, suppressing tether formation (see Fig. 2a). It is noteworthy that the theoretical phase boundaries in Fig. 2a agree very well with the simulation results, which confirms that the relevant mechanisms are captured correctly.

Figure 2b demonstrates that the experimental results are in good qualitative agreement with the simulations, although the simulations exclude the details of the diffusiophoretic particle propulsion and hydrodynamic interactions. Interestingly, for equivalent vesicle conformations, the experimental Pe is typically smaller by a factor of 4–5 than that obtained in the simulations. This could be due to a local spontaneous membrane curvature induced by a local change in lipid concentration, to differences in membrane viscoelasticity or to changes in reorientation time because of particle wrapping by the membrane in the experimental system. We demonstrate that a sufficiently low reduced

volume v lowers the critical value of Pe for the formation of complex tethers. For instance, tethers and daughter vesicles are observed at Pe > 100 for $v \approx 1.0$ (Fig. 2a) and at Pe ≈ 100 for $v = 0.8$, whereas tether-like protrusions appear already at Pe = 50 for $v = 0.6$ (Extended Data Fig. 3). At high particle loadings, vesicle topology changes were observed in the experiments (Extended Data Fig. 5, Supplementary Information), whereas topological changes were not allowed in the simulations (see Methods). We note that in our out-of-equilibrium system, shape and tension can vary dynamically, as demonstrated in Supplementary Video 6, where a cluster of fast-moving ($v_p \approx 21\,\mu m\,s^{-1}$) SPPs leads to the formation of a daughter vesicle, resulting in an increase of tension of the mother vesicle through the active tension induced by SPPs. Figure 2c shows that for a high passive membrane tension ($\lambda_p \approx 25 \pm 9\,\mu N\,m^{-1}$), no visible effects of the activity on the macroscopic vesicle shape are observed under conditions in which flaccid vesicles would show dendritic structures.

Shape fluctuations

In the fluctuating vesicle regime, membrane fluctuation amplitudes are strongly enhanced owing to SPPs compared to the passive case, as demonstrated in Fig. 3a for the experiments. This is reflected both in the larger amplitudes of undulation modes at low mode numbers corresponding to long wavelengths and in the full-width at half-maximum (FWHM) of the probability density function (PDF) $P(\Delta r)$ of the distance Δr between the instantaneous membrane contour and its average position (see inset of Fig. 3a). The simulation results in Fig. 3b show that the FWHM of the PDF increases roughly linearly with Pe. The fluctuations of active vesicles with a volume constraint (with reduced volume close to unity) are smaller than those of vesicles without a volume constraint (Fig. 3b), which can be traced back to the intrinsic membrane tension.

The undulation amplitudes $\langle a_\ell^2 \rangle$ in Fig. 3 show a very good agreement of experimental (Fig. 3a) and simulation (Figs. 3 c, d) results over the entire range of mode numbers ℓ. The spectra can be characterized by two power laws ℓ^α for small and large ℓ values. For passive vesicles with a volume constraint, we find an exponent of $\alpha \approx -1$ for small ℓ (tension-dominated regime) and $\alpha \approx -3$ for larger ℓ (bending-dominated regime), in agreement with earlier observations[20]. For active vesicles, the activity leads to a very pronounced enhancement of the small-ℓ modes, with exponent $\alpha \approx -4$, whereas the bending-dominated regime remains essentially unaffected. We also observe a similar activity-induced power-law regime in our two-dimensional vesicle model, which applies in the limit of strongly flattened vesicle shapes, as shown in Extended Data Fig. 6 (see also Supplementary Information). With increasing ϕ, the density and thickness of the particle layer increase, generating larger active forces on the membrane. This leads to an increase in the fluctuation amplitudes at large ϕ (see Fig. 3c, d), which is reflected in a more negative exponent α in the fluctuation spectrum (see Fig. 3d). However, this increase is moderate because it is opposed by a larger induced membrane tension. We note that the enhancement of activity-induced membrane undulations in our entirely synthetic system is in agreement with previously reported experiments for vesicles with light-activated membrane pumps[24], bacteria encapsulated[25] in GUVs, and for red blood cells with ATP-dependent cytoskeletal activity[26].

Our study shows how the interplay of local active forces, membrane elasticity and viscosity can give rise to a plethora of novel vesicle shapes, which do not exist in equilibrium systems. Notably, further analysis of the strongly distorted vesicle shapes can provide a framework to study non-equilibrium thermodynamic and rheological responses of bilayer membranes when the membrane composition becomes more complex.

Online content

Any methods, additional references, Nature Research reporting summaries, source data, extended data, supplementary information, acknowledgements, peer review information; details of author contributions and competing interests; and statements of data and code availability are available at https://doi.org/10.1038/s41586-020-2730-x.

1. Mattila, P. K. & Lappalainen, P. Filopodia: molecular architecture and cellular functions. *Nat. Rev. Mol. Cell Biol.* **9**, 446–454 (2008).
2. Fletcher, D. A. & Mullins, R. D. Cell mechanics and the cytoskeleton. *Nature* **463**, 485–492 (2010).
3. Needleman, D. & Dogic, Z. Active matter at the interface between materials science and cell biology. *Nat. Rev. Mater.* **2**, 17048 (2017).
4. Turlier, H. et al. Equilibrium physics breakdown reveals the active nature of red blood cell flickering. *Nat. Phys.* **12**, 513–519 (2016).
5. Pizarro-Cerdá, J., Charbit, A., Enninga, J., Lafont, F. & Cossart, P. in *Seminars in Cell & Developmental Biology* Vol. 60, 155–167 (Elsevier, 2016).
6. Dimova, R. & Marques, C. *The Giant Vesicle Book* (CRC Press, 2019).
7. Keber, F. C. et al. Topology and dynamics of active nematic vesicles. *Science* **345**, 1135–1139 (2014).
8. Mulla, Y., Aufderhorst-Roberts, A. & Koenderink, G. H. Shaping up synthetic cells. *Phys. Biol.* **15**, 041001 (2018).
9. Steinkühler, J. et al. Controlled division of cell-sized vesicles by low densities of membrane-bound proteins. *Nat. Commun.* **11**, 905 (2020).
10. Ganzinger, K. A. & Schwille, P. More from less—bottom-up reconstitution of cell biology. *J. Cell Sci.* **132**, 227488 (2019).
11. Mellouli, S. et al. Self-organization of the bacterial cell-division protein Ftsz in confined environments. *Soft Matter* **9**, 10493–10500 (2013).
12. Elgeti, J. & Gompper, G. Wall accumulation of self-propelled spheres. *Eur. Phys. Lett.* **101**, 48003 (2013).
13. Fily, Y., Baskaran, A. & Hagan, M. F. Dynamics of self-propelled particles under strong confinement. *Soft Matter* **10**, 5609 (2014).
14. Bechinger, C. et al. Active particles in complex and crowded environments. *Rev. Mod. Phys.* **88**, 045006 (2016).
15. Gompper, G. et al. The 2019 motile active matter roadmap. *J. Phys. Condens. Matter* **32**, 193001 (2020).
16. Paoluzzi, M., Di Leonardo, R., Marchetti, M. C. & Angelani, L. Shape and displacement fluctuations in soft vesicles filled by active particles. *Sci. Rep.* **6**, 34146 (2016).
17. Wang, C., Guo, Y.-k., Tian, W.-d. & Chen, K. Shape transformation and manipulation of a vesicle by active particles. *J. Chem. Phys.* **150**, 044907 (2019).
18. Li, Y. & ten Wolde, P. Shape transformations of vesicles induced by swim pressure. *Phys. Rev. Lett.* **123**, 148003 (2019).
19. Kroll, D. & Gompper, G. The conformation of fluid membranes: Monte Carlo simulations. *Science* **255**, 968 (1992).
20. Pécréaux, J., Döbereiner, H.-G., Prost, J., Joanny, J.-F. & Bassereau, P. Refined contour analysis of giant unilamellar vesicles. *Eur. Phys. J. E* **13**, 277–290 (2004).
21. Heinrich, V. & Waugh, R. E. A piconewton force transducer and its application to measurement of the bending stiffness of phospholipid membranes. *Ann. Biomed. Eng.* **24**, 595–605 (1996).
22. Cuvelier, D., Derenyi, I., Bassereau, P. & Nassoy, P. Coalescence of membrane tethers: experiments, theory, and applications. *Biophys. J.* **88**, 2714–2726 (2005).
23. Takatori, S. C., Yan, W. & Brady, J. F. Swim pressure: stress generation in active matter. *Phys. Rev. Lett.* **113**, 028103 (2014).
24. Manneville, J.-B., Bassereau, P., Lévy, D. & Prost, J. Activity of transmembrane proteins induces magnification of shape fluctuations of lipid membranes. *Phys. Rev. Lett.* **82**, 4356–4359 (1999).
25. Takatori, S. C. & Sahu, A. Active contact forces drive nonequilibrium fluctuations in membrane vesicles. *Phys. Rev. Lett.* **124**, 158102 (2020).
26. Park, Y. et al. Metabolic remodelling of the human red blood cell membrane. *Proc. Natl Acad. Sci. USA* **107**, 1289–1294 (2010).

Methods

Production of lipids and vesicles

All chemicals, unless otherwise specified, were used as received. 1,2-dioleoyl-*sn*-glycero-3-phosphocholine (DOPC) and the fluorescent 1,2-dioleoyl-*sn*-glycero-3- phosphoethanolamine-*N*-(lissamine rhodamine B sulfonyl) (ammonium salt) (Liss Rhod PE; excitation wavelength 561 nm), both in chloroform, were obtained from Avanti Polar Lipids (Alabaster, AL). Both non-fluorescently labelled DOPC and fluorescently labelled Liss Rhod PE were diluted in chloroform to 12 mg ml^{-1} and 0.2 mg ml^{-1}, respectively, and these stock solutions were stored at −20° C before use. To prepare the lipids in oil solution (LOS), 0.62 g and 0.19 g of DOPC and Liss Rhod PE stock solution (15 mM and 0.15 mM of DOPC and Liss Rhod PE, respectively) were added to a glass vial (20 ml; Infochroma AG). The chloroform was then evaporated under a gentle N_2 gas flow. The lipids were further dried at low pressure in a vacuum desiccator for 3 h to remove any traces of chloroform. Next, 4.4 g (5 ml) of paraffin oil (0.879 g cm^{-3}; EGT Chemie AG) was added, and the lipids were dissolved overnight in an oven at 55° C.

Vesicles were prepared using the modified protocol of Natsume et al.[27], as schematically depicted in Extended Data Fig. 1a. To maintain a density difference between the interior and exterior of the vesicles, the inner and outer aqueous solutions contained 100 mM of sucrose (Sigma-Aldrich) and 100 mM glucose (Apollo Scientific), respectively. The sucrose and glucose solutions were filtered before use with a 0.2-µm Acrodisc filter (Pall Corporation). 600 µl of pre-heated LOS was then added to the 100 µl inner aqueous solution and the two phases were thoroughly mixed by tapping with a 200-µl micropipette for 2 min, giving rise to a water-in-oil emulsion that appeared turbid by eye. In a second 2-ml Eppendorf tube, a lipid-saturated water–oil interface was formed by depositing 200 µl of pre-heated LOS on top of 500 µL of 100 mM glucose solution, the outer aqueous solution. Next, 90–100 µl of the top layer of the emulsion was transferred to the pre-equilibrated interface. The droplets were then transferred through the interface by centrifugation (Eppendorf, 5415D) of the Eppendorf tube for 2 min at 200*g*. The lower centrifugation speed was found to minimize the presence of undesired lipid aggregates in the outer aqueous solution of the vesicle suspension. After centrifugation, the oil phase on top of the aqueous phase was carefully removed with a micropipette. The density difference between the inner and outer aqueous phases ensured that the vesicles had accumulated at the bottom of the tube. The resulting dispersion contained vesicles with sizes ranging between 10 and 80 µm. Extended Data Fig. 1b shows a confocal image of vesicles with a different tension. This method gives an array of vesicles with differing tension, enabling us to explore the effect of this parameter.

Although not mentioned in the literature, the solubility of lipids in different oils (for example, mineral and paraffin oil) at room temperature is known to be poor. Confocal microscope images confirmed the presence of fluorescent aggregates of lipids at room temperature. We found that the solubility of lipids in paraffin oil is good at an elevated temperature (55° C). Cooling the LOS before the formation of the vesicles resulted in the presence of non-uniformities in the vesicle membrane, such as random aggregates of lipids attached to the outer lipid layer of the vesicles. It is therefore essential to keep the LOS at 55° C until use and to minimize the time required for the formation of vesicles.

Fabrication of self-propelling particles

We synthesized polystyrene particles that were sterically stabilized with poly-vinylpyrrolidone (molecular weight M_{wt} = 40,000 kg mol^{-1}) and fluorescently labelled with rhodamine isothiocyanate, using the method of Song et al.[28]. After the synthesis, the particles were washed several times and re-dispersed into Milli-Q water. The particle size was 1.0 µm with a size polydispersity of 5%, as determined using static light scattering and scanning electron microscopy.

To obtain half Pt-coated Janus PS particles, first a monolayer was deposited on a glass slide. Prior to the deposition, the glass slide was rinsed several times with acetone and ethanol, dried under compressed air, and subsequently plasma-cleaned for 30 s at high radio frequency level (Harrick Plasma). Then, 100 µl of dispersion of 0.5 wt% fluorescent PS particles was coated on the slide using a spin-coater (model WS-400B-6NPP Lite; Laurell Technologies) operating in a three-step program (30 s at 400 rpm, 90 s at 1,000 rpm, 20 s at 4,500 rpm). Platinum was then sputter-coated (Safematic, CCU-010 HV Compact Coating) vertically over the monolayer to a final thickness of 5–6 nm. Finally, particles were released from the glass slide by sonication (Bandelin, Sonorex) for approximately 2 min and collected by sedimentation[29].

Next, particles were washed 3–4 times by sedimentation with deionized water to remove small freely floating Pt flakes and unwanted clusters of particles, and then the suspension was diluted to the desired concentration. Before the encapsulation of particles into vesicles, the Janus particles were tested for self-propulsion by diluting the particles in suspensions of varying hydrogen peroxide (BASF) concentrations (0.5–6.0 vol%); see Supplementary Information.

Encapsulation of SPPs

For a typical experiment, 50 µl of Janus particle dispersion of known concentration was mixed with 50 µl of 0.2 M sucrose solution in a 2-ml Eppendorf tube. The composition of this inner aqueous solution could be varied, but the final sucrose concentration was always maintained at 100 mM to prevent osmotic effects across the lipid membrane. Both passive colloids and Janus SPPs were successfully encapsulated into the vesicles, as shown in Extended Data Fig. 1c–f. A combined confocal and bright-field microscope image reveals the two-faced nature of the coated particles (Extended Data Fig. 1e, f), with the fluorescent part appearing bright and the platinum-coated part appearing dark. We note that all the resulting vesicles may not get the same loading of Janus particles.

These encapsulated passive PS Janus particles neither showed a specific interaction with the lipid membrane nor did they induce a substantial change in the vesicle's shape due to mere confinement of the particles, as shown in Extended Data Fig. 1c–f. Moreover, time-lapsed confocal microscope images confirm that the passive particles (that is, without H_2O_2) do not show any specific interactions with the membrane, thus inducing no shape change in vesicles. At low particle loadings, vesicles showed the expected thermal fluctuations of the membrane, of the same intensity as particle-free vesicles, whereas at very high particle loadings, thermal fluctuations were suppressed owing to steric interactions between the membrane and densely packed particles (see Extended Data Fig. 1g–i).

Imaging

We followed the particle dynamics and the membrane fluctuations using a confocal scanning laser microscope (Nikon Eclipse Ti-E inverted microscope with a VT-iSIM confocal scan head, Visitec), a Leica SP8 (Leica Microsystems) confocal scanning laser microscope and a Nikon inverted fluorescence microscope equipped with a Hamamatsu ORCA-Flash4.0 CMOS camera and a high-numerical-aperture (NA) oil objective lens (60×, NA = 1.4; 100×, NA = 1.45). We acquired images with a frame rate in the range of 5–100 frames per second. We acquired a total of 2,500–4,000 images per vesicle for bending rigidity and tension measurements of vesicles by shape fluctuation analysis (see Methods section 'Analysis of shape fluctuations of passive and active vesicles'). The brightness and contrast of the images were adjusted using Fiji imaging software (https://imagej.net/Fiji).

Analysis of shape fluctuations of passive and active vesicles

Vesicle shape fluctuation analysis is a standard technique to extract mechanical membrane properties such as bending rigidity and

tension[20,30,31]. Fluctuation-mode amplitudes $\{a_\ell\}$ for two-dimensional (2D) sections of the vesicle contour, extracted from a contour analysis of experimental and simulation snapshots, are obtained by decomposing the local membrane position $r(\theta_m)$ as

$$a_\ell = \frac{1}{n}\sum_{m=0}^{n-1} r(\theta_m)\exp\left(-\frac{2\pi i \ell m}{n}\right) \quad (1)$$

where ℓ is the mode number and $\theta_m = 2\pi m/n$. In thermal equilibrium, the fluctuation spectra for 2D sections of the vesicle contour are given by[20,30–32]

$$\langle |a_\ell|^2\rangle = \frac{k_B T}{2\lambda_p L}\left(\frac{1}{q_\ell} - \frac{1}{\sqrt{\frac{\lambda_p}{\kappa_c} + q_\ell^2}}\right) \quad (2)$$

where $L = 2\pi\langle R\rangle$ is the section circumference and $q_\ell = \ell/\langle R\rangle$ is the wave number.

For the analysis of the experimental data, a custom-made Matlab program was implemented to detect the membrane contour. First, all images are pre-processed to remove the background noise using a Matlab filter. Second, the membrane contour is detected by drawing a series of radial lines at angles θ_m, and the contour positions are determined by the intensity maximum along the radial lines using a threshold value (see Supplementary Information and Supplementary Fig. 1). The identified positions are transformed from Cartesian coordinates (x_m, y_m), $m = 0,\ldots, n-1$ into polar coordinates $r(\theta_m)$ with respect to the centre of mass of the contour. For the analysis of three-dimensional (3D) simulations, the values of $r(\theta_m)$ at the vesicle cross-section are obtained by local surface interpolation for angles θ_m within the section plane. For 2D simulations, the radial positions of membrane vertices are directly used in the fluctuation analysis.

For both simulations and experiments, we determine the average radius $\langle R\rangle$ of the 2D contours. The complex Fourier amplitudes are evaluated for the membrane position field (equation (1)) using the open-source FFTW library[33] and averaged over different time frames. We note that this analysis of fluctuation modes is performed for both passive and active vesicles. We also quantify the deviations of vesicle shape from a sphere by measuring the PDF $P(\Delta r)$ of the distance Δr from its average shape for both passive and active vesicles; see insets in Fig. 3a, b. The PDFs of both passive and active vesicles show Gaussian-like distributions, in which active vesicles exhibit a larger standard deviation (that is, stronger membrane fluctuations) than passive vesicles.

We extract both the bending rigidity and the tension of the membrane by fitting the experimental fluctuation spectra with equation (2), yielding a membrane tension of $\lambda_p = 13 \pm 7$ nN m^{-1} and a bending rigidity of $\kappa_c = (18 \pm 6)k_B T$ for low-tension vesicles and $\lambda_p = 25 \pm 9$ μN m^{-1}, $\kappa_c = (21 \pm 5)k_B T$ for high-tension vesicles.

Triangulated membrane model of a 3D vesicle

A lipid membrane is modelled by a dynamically triangulated network of N_v linked vertices[19,34]. The links are represented by a tethering potential[34,35] expressed as a combination of the attractive (U_{att}) and repulsive (U_{rep}) parts

$$U_{att}(r) = \begin{cases} k_b \dfrac{\exp[1/(l_{c0}-r)]}{l_{max}-r} & \text{if } r > l_{c0} \\ 0 & \text{if } r \le l_{c0} \end{cases}, \quad (3)$$

$$U_{rep}(r) = \begin{cases} k_b \dfrac{\exp[1/(r-l_{c1})]}{r-l_{min}} & \text{if } r < l_{c1} \\ 0 & \text{if } r \ge l_{c1} \end{cases}, \quad (4)$$

where k_b is the bond stiffness, l_{min} and l_{max} are the minimum and maximum bond lengths, respectively, and l_{c1} and l_{c0} are the potential cutoff lengths. Thus, membrane vertices can move freely in the range $[l_{c1}, l_{c0}]$.

The bending elasticity is represented by the Helfrich curvature energy[36] as

$$U_{bend} = 2\kappa_c \oint_A \bar{c}^2 dA, \quad (5)$$

where κ_c is the bending rigidity, $\bar{c} = (c_1 + c_2)/2$ is the local mean curvature and A is the total membrane area. The bending energy is discretized on a triangulated network[37,38] as

$$U_{bend} = \sum_{i=1}^{N_v} \frac{2\kappa_c \bar{c}_i^2 A}{N_v} = \frac{\kappa_c}{2}\sum_{i=1}^{N_v}\frac{1}{\sigma_i}\left[\mathbf{n}_i \cdot \left(\sum_{j(i)}\frac{\sigma_{ij}}{r_{ij}}\mathbf{r}_{ij}\right)\right]^2, \quad (6)$$

where $\bar{c}_i$ is the mean curvature at vertex i with area A/N_v; $\mathbf{n}_i$ is the unit normal of the membrane at vertex i; $\sigma_i = (\sum_{j(i)} \sigma_{ij} r_{ij})/4$ is the area of a dual cell of vertex i; $j(i)$ stands for all neighbouring vertices linked to vertex i; and $\sigma_{ij} = r_{ij}(\cot\theta_1 + \cot\theta_2)/2$ is the length of the bond in a dual lattice with angles θ_1 and θ_2 at the vertices opposite to the shared bond vector $\mathbf{r}_{ij}$. More details about the discretization of the Helfrich curvature energy can be found in refs. [34,37,39].

Furthermore, local area conservation of the triangles in the vesicle discretization is imposed by a soft harmonic potential given by

$$U_{loc.area} = \frac{k_l}{2}\sum_{i=1}^{N_t}\frac{(A_i - A')^2}{A'}, \quad (7)$$

where k_l, $A' = A/N_t$ and A_i are the local-area conservation coefficient, the desired and the instantaneous local areas, respectively. The sum runs over all $N_t = 2(N_v - 2)$ triangles within the network. In several simulations, a constraint on the total vesicle volume V has been employed as

$$U_{volume} = \frac{k_v(V - V_0)^2}{2V_0}, \quad (8)$$

where k_v is the volume constraint coefficient and V_0 is the desired total volume.

The dynamics of membrane vertices is modelled by the Langevin equation,

$$m\ddot{\mathbf{r}}_i = -\nabla_i U_{tot} - \gamma_m \dot{\mathbf{r}}_i + \sqrt{2\gamma_m k_B T}\,\boldsymbol{\xi}_i(t), \quad (9)$$

where m is the vertex mass, $\ddot{\mathbf{r}}_i$ and $\dot{\mathbf{r}}_i$ are the second and first derivatives of particle positions $\mathbf{r}_i$, ∇_i is the spatial derivative at the position of vertex i and U_{tot} is the sum of all interaction potentials. The friction coefficient γ_m mimics the embedding of the membrane into a viscous fluid through the free-draining approximation. $\boldsymbol{\xi}_i(t)$ is a Gaussian random process with $\langle\boldsymbol{\xi}_i(t)\rangle = 0$ and $\langle\boldsymbol{\xi}_i(t)\boldsymbol{\xi}_j(t')\rangle = \mathbb{I}_d\delta_{ij}\delta(t-t')$ that represents membrane thermal fluctuations (where $\mathbb{I}_d$ is the $d \times d$ identity matrix and d is the dimension). The positions and velocities of all particles are integrated using the velocity Verlet algorithm[40].

Membrane fluidity: dynamic triangulation

The membrane model described above with a fixed network connectivity does not include membrane fluidity, in which particles can diffuse within the membrane plane. To model membrane fluidity, the bond shared by each pair of adjacent triangles is flipped to connect the two previously unconnected vertices[34,38]. The flipping procedure is performed with a time frequency of ω. During the flipping procedure, every bond in the membrane network is flipped with probability ψ, where the acceptance of bond flipping follows a Monte Carlo algorithm. In the Monte Carlo algorithm, changes in the tethering (that is, $\Delta U_{att} + \Delta U_{rep}$) and local area (that is, $\Delta U_{loc.area}$) energies due to attempted bond

flipping are computed. Bond flipping is accepted with a probability of $\exp[-(\Delta U_{att} + \Delta U_{rep} + \Delta U_{loc.area})/(k_B T)]$ if energetically unfavourable and is always accepted if energetically favourable. We note that a change in the bending energy is omitted here for numerical efficiency, as bond flipping has a negligible effect on the local membrane curvature. The resulting membrane fluidity for selected parameters ω and ψ can be characterized by a 2D membrane viscosity; see refs. [35,41] for details. Extended Data Table 1 outlines the parameters for the 3D simulations.

Semiflexible-ring model of a 2D vesicle

A 2D cross-section (or a cut) of a vesicle is modelled by a semiflexible polymer ring. The ring is composed of N_r beads and characterized by a perimeter length of $2\pi R$. The beads interact by bond, bending and area-constraint potentials; however, no repulsion between beads is applied. The bond energy controls the length of the polymer ring both locally and globally, and is represented by a harmonic bond potential

$$U_s = \frac{k_s}{2} \sum_{i=0}^{N_r-1} (|\mathbf{r}_i| - l_s)^2 \tag{10}$$

Here, k_s is the spring constant, $l_s = 2R\sin(\pi/N_r)$ is the equilibrium bond length, and $\mathbf{r}_i$ is the bond vector from monomer i to $i+1$. The spring constant k_s is chosen sufficiently large, such that changes in the ring perimeter length are less than 5%.

The curvature (or bending) energy

$$U_b = \frac{\kappa'}{l_s} \sum_{i=0}^{N_r-1} (1 - \cos\theta_i) \tag{11}$$

controls the membrane deformation in two dimensions. Here, κ' is the 2D bending rigidity and θ_i is the angle between bond vectors $\mathbf{r}_i$ and $\mathbf{r}_{i+1}$. Finally, the area compression energy

$$U_A = \frac{k_A}{2}(A - A_0)^2 \tag{12}$$

controls the area enclosed by the polymer ring, which mimics volume conservation of a vesicle in three dimensions. Here, k_A is the bulk modulus, and A and A_0 are the instantaneous and the target ring areas, respectively. Similarly to the 3D simulations, the dynamics of deformable rings is governed by the Langevin equation (9) in two dimensions. Extended Data Table 2 summarizes the parameters for the 2D simulations.

Model of SPPs

Self-propelled Janus particles are modelled by active Brownian particles (ABPs) without hydrodynamic interactions. Each ABP experiences a propulsive force f_p, such that the average propulsive velocity of an ABP can be estimated as $\langle v_p \rangle = f_p/\gamma_p$, where $\gamma_p = 3\pi\eta_f\sigma$ is the friction coefficient for ABPs with a diameter σ and η_f is the fluid dynamic viscosity. The propulsive force $f_p\mathbf{e}_i$ is added to the Langevin dynamics in equation (9), where $\mathbf{e}_i$ is the unit orientation vector of the i-th ABP. In addition, the orientation vector is subject to a random rotation following the equation[42,43] $\dot{\mathbf{e}}_i = \boldsymbol{\zeta}_i \times \mathbf{e}_i$, where $\boldsymbol{\zeta}_i(t)$ is a Gaussian random process with $\langle \boldsymbol{\zeta}_i(t) \rangle = 0$ and $\langle \boldsymbol{\zeta}_i(t)\boldsymbol{\zeta}_j(t') \rangle = 2D_r\mathbb{I}_d\delta_{ij}\delta(t-t')$ with rotational diffusion coefficient D_r of an ABP. D_r is related to the ABP size σ and its translational diffusion $D_t = k_B T/\gamma_p$ as $D_t = D_r\sigma^2/3$. The activity of ABPs is characterized by the dimensionless Péclet number $\mathrm{Pe} = \sigma v_p/D_t$.

ABPs repel each other with the repulsive part of the 12-6 Lennard–Jones (LJ) potential given by

$$U_{pair}(r) = \begin{cases} \epsilon\left[\left(\frac{r_c^p}{r}\right)^{12} - 2\left(\frac{r_c^p}{r}\right)^{6}\right] & \text{if } r < \sqrt[6]{2}\, r_c^p \\ 0 & \text{if } r \geq \sqrt[6]{2}\, r_c^p \end{cases}, \tag{13}$$

where ϵ is the strength of the LJ potential and r_c^p is a characteristic length of repulsion. Thus, for ABPs we set $r_c^p = \sigma$. Similarly, ABPs are also repelled by membrane vertices, and this interaction is described by the repulsive part of the LJ potential with $r_c^p = 0.5\sigma$. The ABP parameters used in the simulations can be found in Extended Data Tables 1, 2.

Analytical prediction for the onset of tether formation

Tether formation from vesicles by externally pulled passive colloidal particles has been studied intensively[21,22]. We adopt here a simplified version of the theoretical description of this process to tether formation by several active particles inside a vesicle. Tether formation occurs through the propulsion force f_p exerted by a single particle or through the force

$$f_{p,c} = \beta N_{p,c} f_p = \beta N_{p,c} \frac{\mathrm{Pe} k_B T}{\sigma} \tag{14}$$

exerted by a cluster of $N_{p,c}$ particles on the membrane. Here, $\beta \leq 1$ is the cluster cooperativity coefficient, which measures orientation alignment of the propulsion directions.

We consider a membrane with bending rigidity κ_c and spontaneous curvature c_0. The propulsion force must overcome an elastic membrane force

$$f_{tether} = \pi\sigma_{cl}\left(\lambda + \frac{2\kappa_c}{\sigma_{cl}^2} - \frac{4\kappa_c c_0}{\sigma_{cl}}\right) \tag{15}$$

to pull a tether of a diameter σ_{cl}, which represents the effective cluster size. Here, the membrane tension λ contains contributions from both the passive (equilibrium) tension of the vesicle, λ_p, and the tension induced by the particle activity, λ_a; that is, $\lambda = \lambda_p + \lambda_a$. For vesicles containing many SPPs, tether formation can thus be enhanced by cluster formation and spontaneous membrane curvature, and be suppressed by membrane tension.

In the stationary state, a tether radius is predicted by minimizing the elastic energy of a vesicle with N tethers as

$$R_t = \frac{\pi\kappa_c}{f_{p,c}} \tag{16}$$

with a fixed membrane area $A_{tot} = 4\pi R^2 + 4\pi N R_t L_t$ and tether length L_t. We note that this radius is independent of the number of tethers.

To predict the boundary of tether formation in the state diagram by equation (15), estimates of the cluster size $N_{p,c}$ and the activity-induced tension are required. We estimate the average cluster size $\langle N_{p,c} \rangle$ from the simulated distributions of cluster sizes illustrated in Extended Data Fig. 4a. Our simulation data for Pe = 100 show that

$$\langle N_{p,c} \rangle \approx \alpha N_p, \tag{17}$$

where α is a monotonically increasing function of Pe, with $\alpha \approx 1.9 \times 10^{-2}$ for Pe = 100. Then, the cluster size is assumed to be $\sigma_{cl} = \sigma(\langle N_{p,c} \rangle/\nu_{cl})^{1/3}$, where $\nu_{cl} = 0.65$ represents the packing fraction of the cluster. The active membrane tension λ_a originates from the swim pressure that the particles exert on the membrane. It can be estimated through the Young–Laplace equation as

$$\lambda_a = \gamma \frac{N_p f_p}{8\pi R}, \tag{18}$$

where $\gamma \leq 1$ is the active-tension weight, which takes into account that not all SPPs exert a force perpendicular to the membrane. As a result, the force balance implies a critical Péclet number for tether formation of

$$\mathrm{Pe}_c = \frac{\pi\sigma}{k_B T}\left(\sigma_{cl}\lambda_p + \frac{2\kappa_c}{\sigma_{cl}} - 4\kappa_c c_0\right)\left(\beta\langle N_{p,c}\rangle - \gamma\frac{N_p}{8}\frac{\sigma_{cl}}{R}\right)^{-1}. \quad (19)$$

Extended Data Figure 7 compares phase boundaries calculated using equation (19) for various values of λ_p, β and c_0.

Data availability

The data that support the findings of this study are available from the corresponding authors upon reasonable request.

Code availability

The codes used in this study are available from the corresponding authors upon reasonable request.

27. Natsume, Y. et al. Preparation of giant vesicles encapsulating microspheres by centrifugation of a water-in-oil emulsion. *J. Vis. Exp.* **119**, e55282 (2017).
28. Song, J.-S., Tronc, F. & Winnik, M. A. Two-stage dispersion polymerization toward monodisperse, controlled micrometre-sized copolymer particles. *J. Am. Chem. Soc.* **126**, 6562–6563 (2004).
29. Vutukuri, H. R., Bet, B., Van Roij, R., Dijkstra, M. & Huck, W. T. Rational design and dynamics of self-propelled colloidal bead chains: from rotators to flagella. *Sci. Rep.* **7**, 16758 (2017).
30. Drabik, D., Przybyło, M., Chodaczek, G., Iglič, A. & Langner, M. The modified fluorescence based vesicle fluctuation spectroscopy technique for determination of lipid bilayer bending properties. *Biochim. Biophys. Acta Biomembr.* **1858**, 244–252 (2016).
31. Yoon, Y.-Z. et al. Flickering analysis of erythrocyte mechanical properties: dependence on oxygenation level, cell shape, and hydration level. *Biophys. J.* **97**, 1606–1615 (2009).
32. Bassereau, P., Sorre, B. & Lévy, A. Bending lipid membranes: experiments after W. Helfrich's model. *Adv. Colloid Interface Sci.* **208**, 47–57 (2014).
33. Frigo, M. & Johnson, S. G. The design and implementation of FFTW3. *Proc. IEEE* **93**, 216–231 (2005).
34. Gompper, G. & Kroll, D. M. in *Statistical Mechanics of Membranes and Surfaces* 2nd edn (eds Nelson, D. R. et al.) 359–426 (World Scientific, 2004).
35. Noguchi, H. & Gompper, G. Dynamics of fluid vesicles in shear flow: effect of the membrane viscosity and thermal fluctuations. *Phys. Rev. E* **72**, 011901 (2005).
36. Helfrich, W. Elastic properties of lipid bilayers: theory and possible experiments. *Z. Naturforsch. C* **28**, 693–703 (1973).
37. Gompper, G. & Kroll, D. Random surface discretizations and the renormalization of the bending rigidity. *J. Phys. I* **6**, 1305–1320 (1996).
38. Gompper, G. & Kroll, D. M. Network models of fluid, hexatic and polymerized membranes. *J. Phys. Condens. Matter* **9**, 8795–8834 (1997).
39. Guckenberger, A. & Gekle, S. Theory and algorithms to compute Helfrich bending forces: a review. *J. Phys. Condens. Matter* **29**, 203001 (2017).
40. Allen, M. P. & Tildesley, D. J. *Computer Simulation of Liquids* (Clarendon Press, 1991).
41. Noguchi, H. & Gompper, G. Fluid vesicles with viscous membranes in shear flow. *Phys. Rev. Lett.* **93**, 258102 (2004).
42. Wysocki, A., Winkler, R. G. & Gompper, G. Cooperative motion of active Brownian spheres in three-dimensional dense suspensions. *Eur. Phys. Lett.* **105**, 48004 (2014).
43. Stenhammar, J., Marenduzzo, D., Allen, R. J. & Cates, M. E. Phase behaviour of active Brownian particles: the role of dimensionality. *Soft Matter* **10**, 1489–1499 (2014).

Acknowledgements H.R.V. acknowledges financial support through a Marie Skłodowska-Curie Intra European Individual Fellowship (grant number 708349-SPCOLPS) within Horizon 2020. J.V. acknowledges financial support by the Swiss National Science Foundation (grant number 200021-165974). C.A.-V. acknowledges support by the International Helmholtz Research School of Biophysics and Soft Matter (IHRS BioSoft). G.G. acknowledges support by Deutsche Forschungsgemeinschaft (DFG) through the priority programme SPP1726 on 'Microswimmers'. We thank P. Walde for discussions, N. Jaensson for initial help with membrane curve fitting in experiments and E. Spruijt for polystyrene particle synthesis. We gratefully acknowledge the computing time granted through JARA-HPC on the supercomputer JURECA at Forschungszentrum Jülich.

Author contributions H.R.V. and J.V. conceived and designed the project. H.R.V., L.v.B., and A.D. performed the experimental work. H.R.V. performed the experimental analysis. T.A., D.A.F. and G.G. designed the simulations. M.H. and D.A.F. performed 3D simulations. C.A.-V. performed 2D simulations. M.H., C.A.-V. and D.A.F. analysed the simulation data. M.H., C.A.-V, D.A.F. and T.A. performed the analytical calculations. All authors participated in the discussions, and H.R.V., T.A., D.A.F., G.G. and J.V. wrote the manuscript.

Competing interests The authors declare no competing interests.

Additional information
Supplementary information is available for this paper at https://doi.org/10.1038/s41586-020-2730-x.
Correspondence and requests for materials should be addressed to H.R.V. or G.G.
Peer review information *Nature* thanks Rumiana Dimova and the other, anonymous, reviewer(s) for their contribution to the peer review of this work.

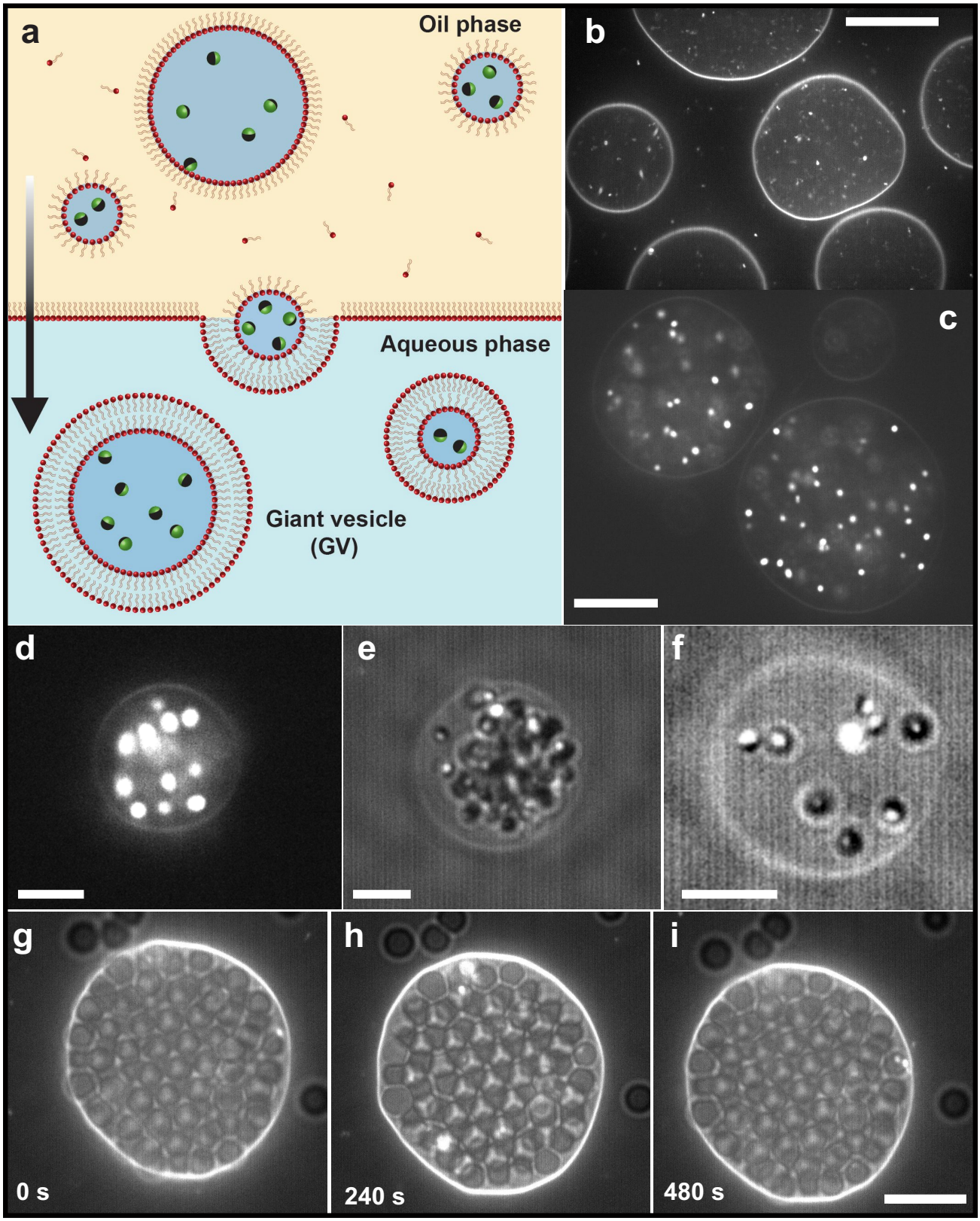

Extended Data Fig. 1 | Encapsulation of colloids in giant DOPC vesicles. **a**, Schematic representation of the working principle of the production of giant vesicles by using the droplet transfer method. **b**–**d**, Confocal microscopy images showing the lipid membrane and particles in GUVs. Passive isotropic particles in low-tension vesicles (**c**) and high-tension giant vesicles (**d**). Combined confocal and bright-field micrographs of Janus particles inside the GUVs of high-tension (**e**) and low-tension (**f**) vesicles. **g**–**i**, Sequence of time-lapse combined 2D confocal and bright-field microscopy images showing no specific interactions between the particles and the lipid membrane; as a result, no vesicle shape change is observed. The particle volume fraction is $\phi \approx 0.23$. Scale bars are 10.0 μm.

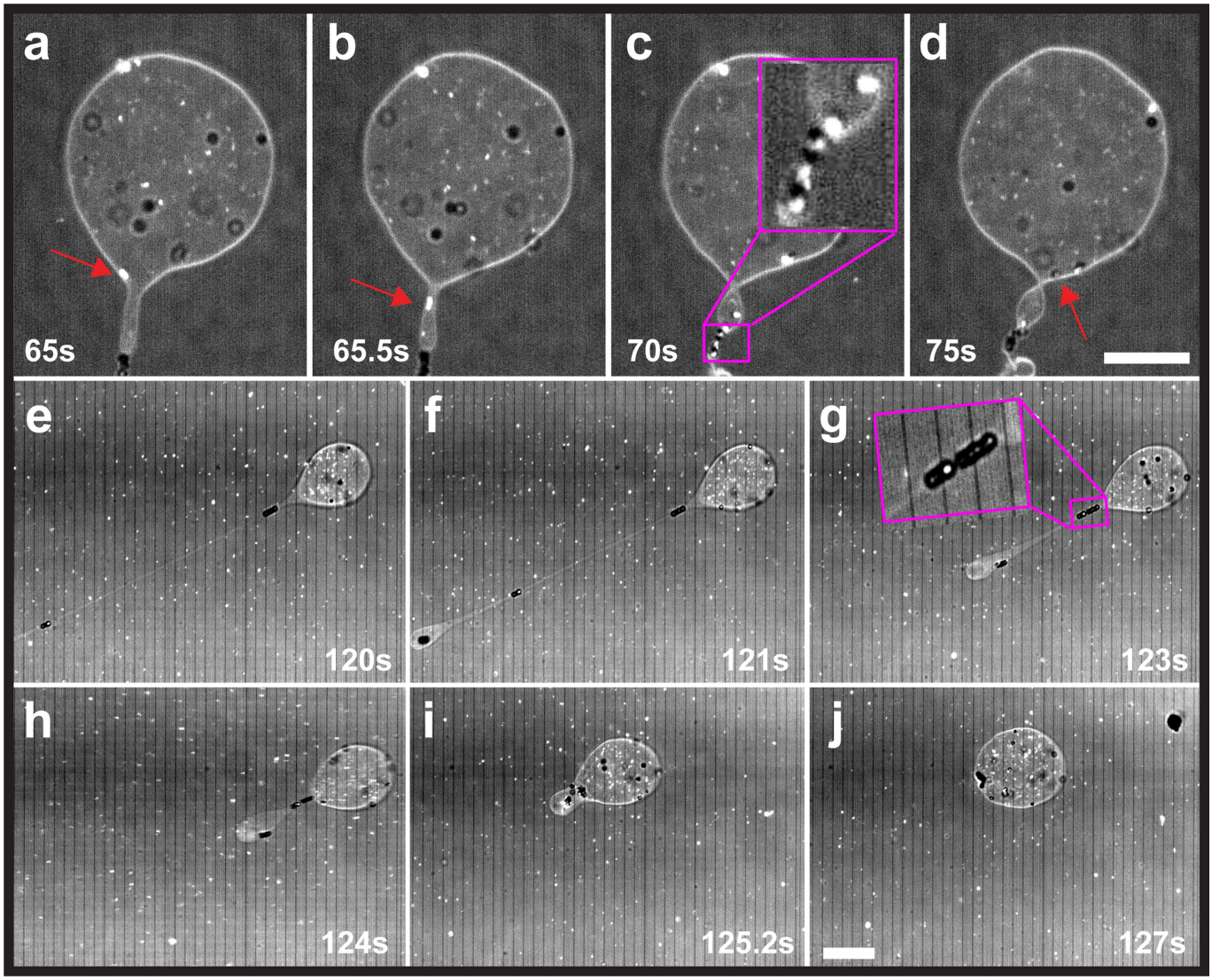

Extended Data Fig. 2 | Cooperative budding and tubular confinement of SPPs. Time-lapse of combined confocal and bright-field microscopy images showing the cooperative motion of SPPs inside the tether/channel of the lipid membrane. **a**–**d**, A flaccid vesicle first shows formation of a tether, which is transformed into a channel by multiple active particles. SPPs move into (**a**, **b**) and out of (**c**, **d**) the channel when they change propulsion direction. The inset shows a helical packing of active particles. The red arrow depicts the direction of the motion of the active particle into and out of the channel. The particle volume fraction is $\approx 3 \times 10^{-3}$. **e**–**j**, Formation of a long (≈200 µm) tether extruded by a cluster of active particles (ten). Time-lapse images show the tubular confinement of a linear arrangement (inset of **g**) of individual active particles while the cluster of particles further pulls the membrane. **h**–**j**, The tether remains stable until its propulsion direction is reversed and the stored elastic energy counteracts the tether formation. As a result, the vesicle recovers its spherical shape. Scale bars are 10.0 µm.

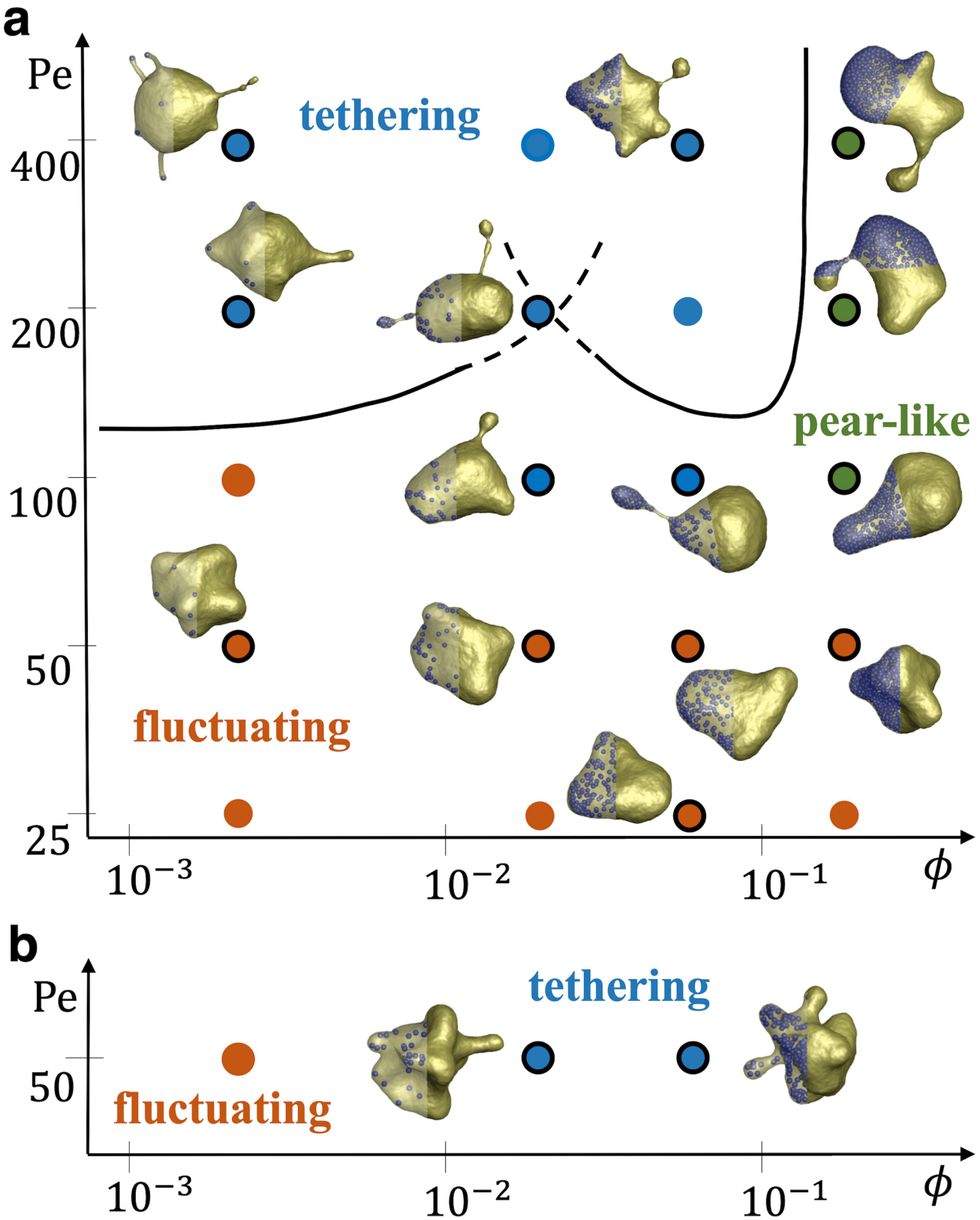

Extended Data Fig. 3 | State diagram of various membrane structures for a vesicle with a volume constraint. a, Vesicle shapes for reduced volume $v = 0.8$ as a function of Pe and ϕ. Similar to the simulated diagram in Fig. 2a for a vesicle without a volume constraint, three regimes exist: tethering (blue symbols), fluctuating (red symbols) and bola/prolate (green symbols) vesicle shapes. The points corresponding to the snapshots have black outlines. The boundary (black lines) of the tethering regime from theoretical calculations is the same as in Fig. 2a. Interestingly, tether formation for $v = 0.8$ is present at Pe = 100, whereas without a volume constraint, tethers and daughter vesicles are observed only for Pe > 100. **b**, Simulations of vesicles deformed by active particles for reduced volume $v = 0.6$ at Pe = 50. The occurrence of protrusions at Pe = 50 demonstrates that low reduced volumes favour the formation of tethers or daughter vesicles.

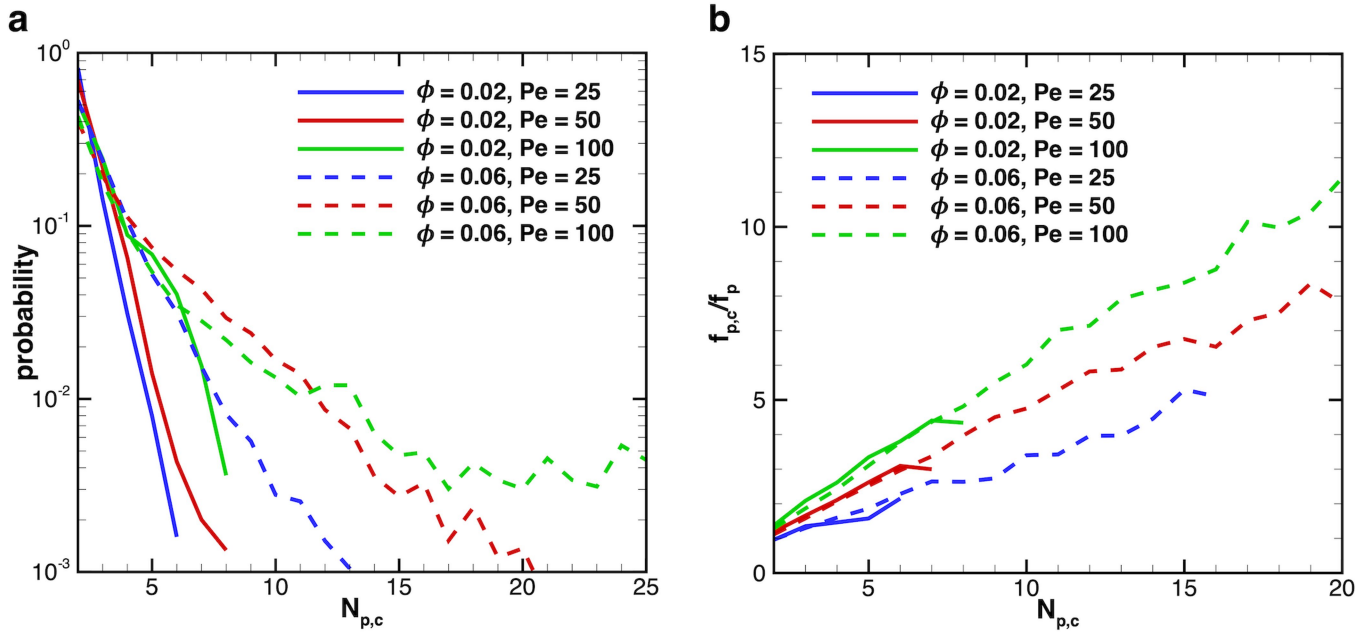

Extended Data Fig. 4 | Sizes and forces of active particle clusters. a, Size distributions of clusters formed by active particles for various Pe and ϕ values from simulations with reduced volume $v = 0.8$. Larger clusters form at higher volume fractions of active particles and at larger Pe. The tails of the cluster size distributions follow a nearly exponential decay. **b**, Average cluster forces in the direction of the membrane for various Pe and ϕ values. The average force is a nearly linear function of the cluster size $N_{p,c}$, such that it can be approximated as $f_{p,c} = \beta N_{p,c} f_p$, where β is the cooperativity coefficient, which weakly depends on Pe. Linear fitting of the $f_{p,c}$ data results in $\beta \approx 0.3$ for Pe = 25, $\beta \approx 0.4$ for Pe = 50 and $\beta \approx 0.54$ for Pe = 100.

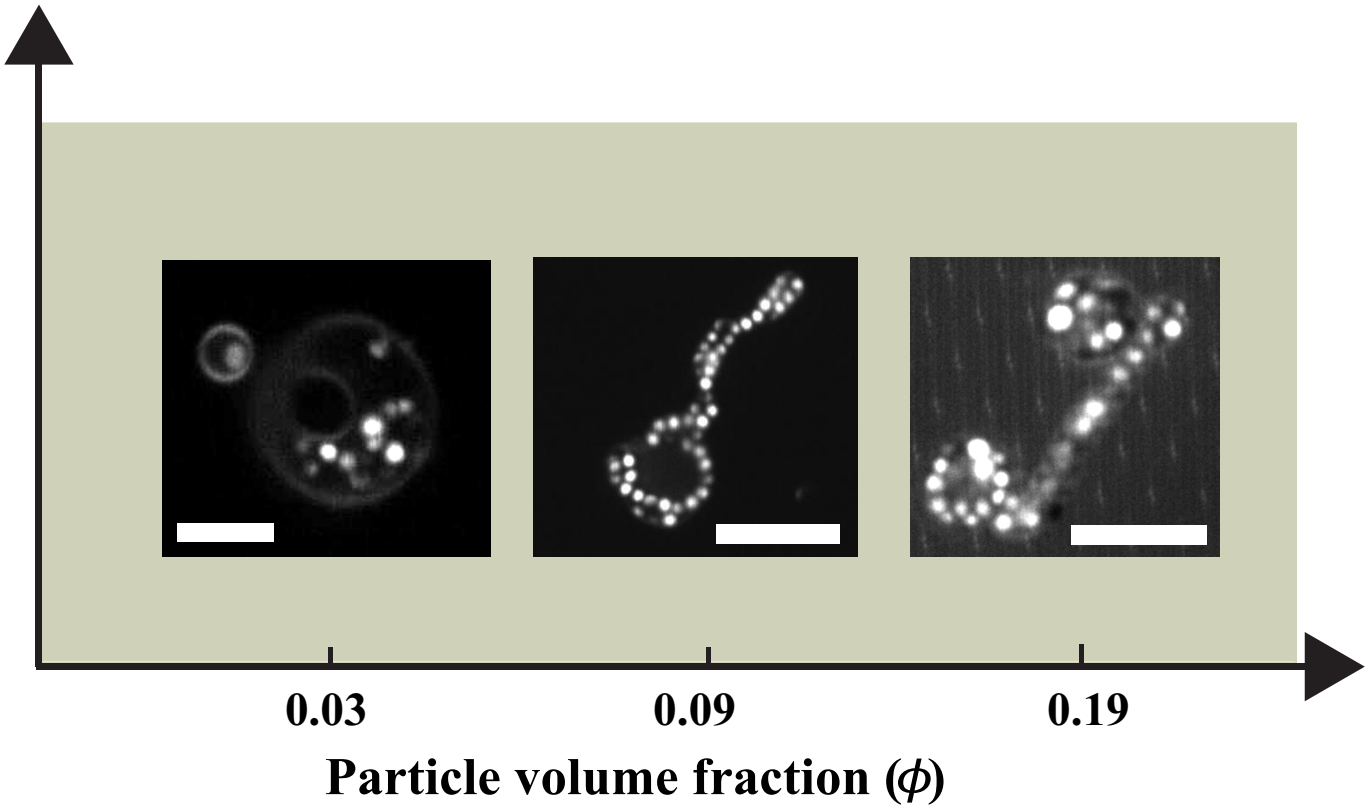

Extended Data Fig. 5 | Vesicle morphologies at higher particle loadings. Vesicle topology changes are observed at high volume fraction of particles. Scale bars are 10.0 μm.

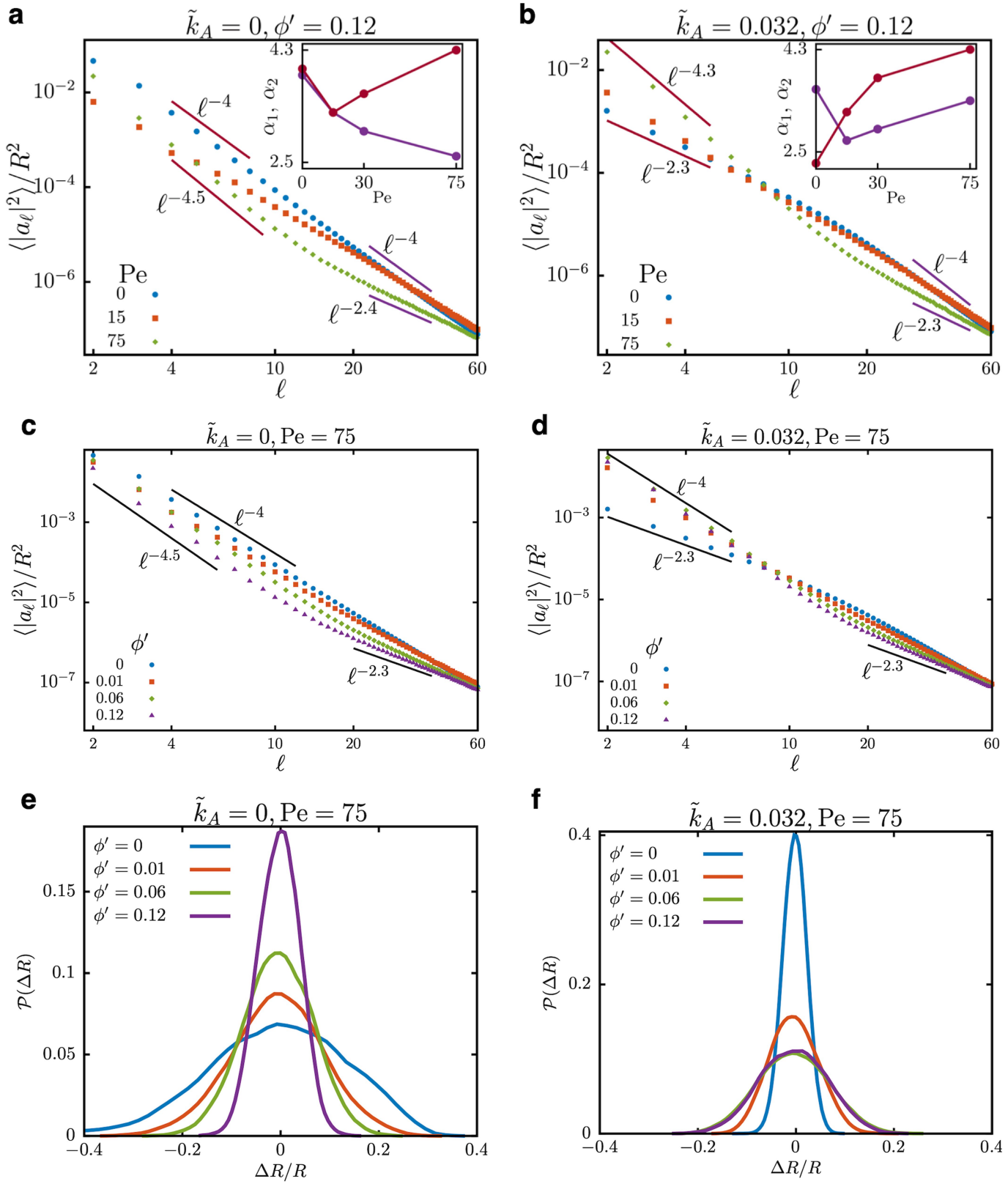

Extended Data Fig. 6 | Fluctuations of 2D vesicles. a, **b**, Fluctuation spectra for vesicles with enclosed active particles of various Pe at area fraction $\phi' = 0.12$ without (**a**) and with (**b**) an area constraint. The insets show the exponents obtained using power-law fits to $\ell^{-\alpha}$, measured in the ranges $10 \le \ell \le 17$ for α_1 and $35 \le \ell \le 50$ for α_2. **c**, **d**, Fluctuation spectra of active vesicles at Pe = 75 for various volume fractions ϕ' without (**c**) and with (**d**) an area constraint. **e**, **f**, PDFs for fluctuations of the radial position of the vesicle contour around its average position for rings without (**e**) and with (**f**) an area constraint. The data denoted by $\phi' = 0$ are for the passive system.

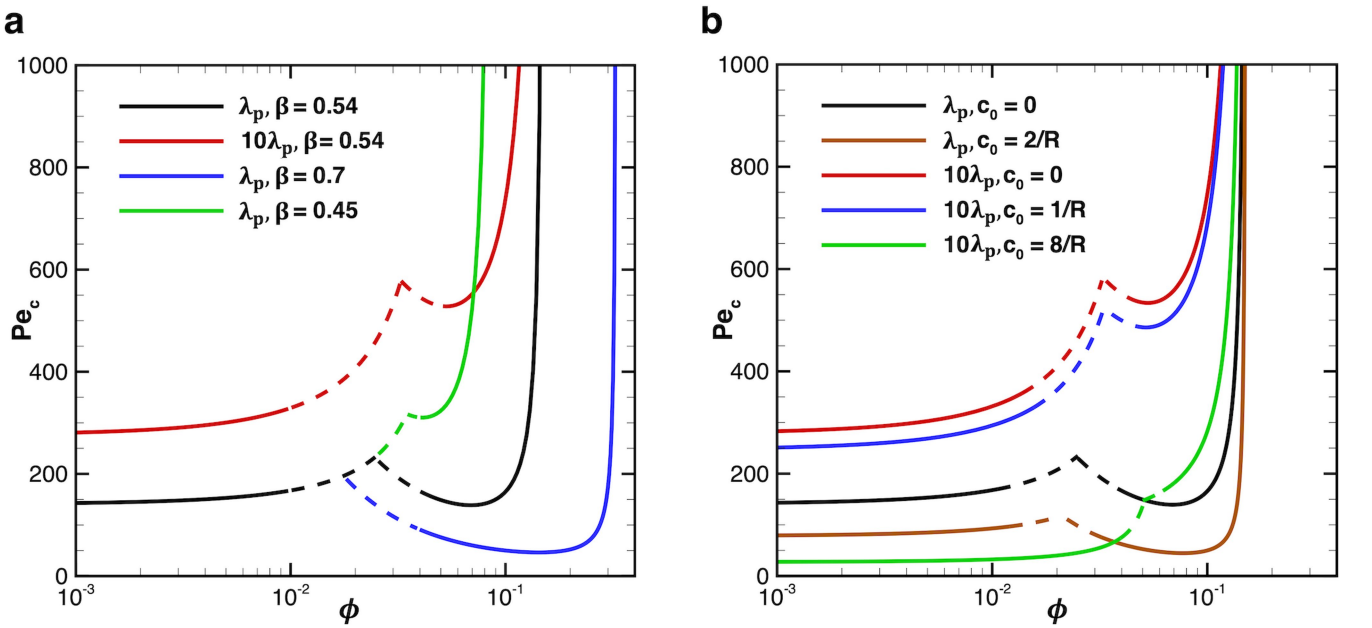

Extended Data Fig. 7 | Theoretical phase diagrams for tether formation by active particles for two passive membrane tensions λ_p. a, Tether boundaries for various cluster cooperativities β. At low ϕ, equation (19) with $\langle N_{p,c}\rangle = 1$, $\beta = 1$ and $\sigma_{cl} = \sigma$ is employed, whereas at large ϕ, $\langle N_{p,c}\rangle$ and σ_{cl} are functions of the number N_p of active particles. In all cases, the active-tension weight is set to $\gamma = 0.25$. **b**, Tether boundaries for different spontaneous curvatures c_0. Here, $\lambda_p = 2 \times 10^{-8}$ N m^{-1}. Tethers are predicted to occur at high enough Pe and for small volume fractions ϕ of active particles. A non-zero spontaneous curvature of the membrane can substantially reduce the propulsion force needed to form a tether.

Extended Data Table 1 | Parameters used in 3D simulations

Parameters	Model units	Physical units
	Principal properties	
vesicle radius in equilibrium R	32	$8\,\mu\mathrm{m}$
thermal energy unit $k_\mathrm{B}T$	0.2	$4.14\times10^{-21}\ \mathrm{J}$
time scale $\tau=\gamma_\mathrm{p}R^2/\kappa_\mathrm{c}$	1.28×10^{5}	$7.3\ \mathrm{s}$
	Investigated properties	
Peclet number $\mathrm{Pe}=\sigma \mathrm{v_p}/\mathrm{D_t}$	$25-800$	$25-800$
total number of SPPs N_p	$3-1458$	$3-1458$
SPP volume fraction $\phi=N_\mathrm{p}\left(\sigma/2R\right)^3$	$7.3\times10^{-4}-3.56\times10^{-1}$	$7.3\times10^{-4}-3.56\times10^{-1}$
SPP diameter σ	$R/8$	$1\,\mu\mathrm{m}$
	Vesicle properties	
number of vertices N_v	$30,000$	$30,000$
bending rigidity κ_c	$20k_\mathrm{B}T$	$8.28\times10^{-20}\ \mathrm{J}$
average bond length l_b	$4R\sqrt{\frac{\pi}{N_\mathrm{t}\sqrt{3}}}$	$0.176\,\mu\mathrm{m}$
bond stiffness k_b	$80k_\mathrm{B}T$	$3.31\times10^{-19}\ \mathrm{J}$
minimum bond length l_min	$0.6l_\mathrm{b}$	$0.11\,\mu\mathrm{m}$
potential cutoff length l_{c1}	$0.8l_\mathrm{b}$	$0.14\,\mu\mathrm{m}$
potential cutoff length l_{c0}	$1.2l_\mathrm{b}$	$0.21\,\mu\mathrm{m}$
maximum bond length l_max	$1.4l_\mathrm{b}$	$0.25\,\mu\mathrm{m}$
desired vesicle area A	$4\pi R^2$	$8.04\times10^{2}\ \mu\mathrm{m}^2$
desired vesicle volume V_0	$4\pi R^3/3$	$2.14\times10^{3}\ \mu\mathrm{m}^3$
local area stiffness k_l	$6.43\times10^{6}\ k_\mathrm{B}T/A$	$3.3\times10^{-5}\ \mathrm{J/m^2}$
volume stiffness k_v (if used)	$1.6\times10^{7}\ k_\mathrm{B}T/R^3$	$130\ \mathrm{J/m^3}$
friction coefficient γ_m	$0.4\ k_\mathrm{B}T\tau/R^2$	$1.9\times10^{-10}\ \mathrm{J\cdot s\cdot m^{-2}}$
flipping frequency ω	$6.4\times10^{6}\ \tau^{-1}$	$8.8\times10^{5}\ \mathrm{s^{-1}}$
flipping probability ψ	0.3	0.3
	SPP properties	
translational friction γ_p	$20\ k_\mathrm{B}T\tau/R^2$	$9.4\times10^{-9}\ \mathrm{J\cdot s\cdot m^{-2}}$
translational diffusion D_t	$k_\mathrm{B}T/\gamma_\mathrm{p}$	$4.4\times10^{-13}\ \mathrm{m^2\cdot s^{-1}}$
rotational diffusion D_r	$3D_\mathrm{t}/\sigma^2$	$1.32\ \mathrm{s^{-1}}$
LJ potential depth ϵ	$2k_\mathrm{B}T$	$8.28\times10^{-21}\ \mathrm{J}$

A set of simulation parameters for 3D vesicle systems in both model and physical units.

Extended Data Table 2 | Parameters used in 2D simulations

Parameters	Model units	Physical units
Principal properties		
vesicle radius in equilibrium R		$16\,\mu\mathrm{m}$
SPP rotational diffusion time $\tau_\mathrm{r} = 1/D_\mathrm{r}$		$3.1\,\mathrm{ms}$
SPP area fraction $\phi' = N_\mathrm{p}\left(\sigma/2R\right)^2$	$0 - 0.12$	$0 - 0.12$
Vesicle properties		
number of vertices N_r	395	395
equilibrium bond length $l_\mathrm{s} = 2\pi R/N_\mathrm{r}$	$0.016\,R$	$0.25\,\mu\mathrm{m}$
bead radius r_c	$0.02\,R$	$0.3\,\mu\mathrm{m}$
inverse bead overlap $\xi = \pi R/(\sigma N_\mathrm{r})$	0.2	0.2
friction coefficient γ_m	$633\,k_BT\tau_\mathrm{r}/R^2$	$2.7 \times 10^{-18}\,\mathrm{Ns/m}$
bond spring constant $k_\mathrm{s} = 1.3 \times 10^4\,k_\mathrm{B}T/l_\mathrm{s}^2$	$5 \times 10^7\,k_BT/\mathrm{R}^2$	$8 \times 10^{-16}\,\mathrm{J/\mu m^2}$
2D bending rigidity κ'	$10\,k_\mathrm{B}TR$	$6.6 \times 10^{-19}\mathrm{J\mu m}$
desired vesicle area $A_0 = \pi R^2$	$3.14\,R^2$	$805\,\mu\mathrm{m}^2$
area compression modulus k_A	$5 \times 10^5\,k_BT/R^4$	$3.2 \times 10^{-20}\,\mathrm{J/\mu m^4}$
reduced area compression modulus $\tilde{k}_\mathrm{A} = k_\mathrm{A}l_\mathrm{s}^4/k_\mathrm{B}T$	0.032	0.032
SPP properties		
diameter σ	$0.06R$	$1\,\mu\mathrm{m}$
Peclet number, $\mathrm{Pe} = \sigma \mathrm{v_p}/\mathrm{D_t}$	$0 - 150$	$0 - 150$
translational friction γ_p	$1000\,k_BT\tau_\mathrm{r}/R^2$	$4.3 \times 10^{-18}\,\mathrm{Ns/m}$
rotational friction $\gamma_\mathrm{r} = \gamma_\mathrm{p}\sigma^2/3$	$k_BT\tau_\mathrm{r}$	$1.3 \times 10^{-18}\,\mathrm{Js}$
translational diffusion $D_\mathrm{t} = k_\mathrm{B}T/\gamma_\mathrm{p}$	$0.001\,R^2/\tau_\mathrm{r}$	$10^{-3}\,\mu\mathrm{m}^2/\mathrm{s}$
rotational diffusion $D_\mathrm{r} = k_\mathrm{B}T/\gamma_\mathrm{r}$	τ_r^{-1}	$320\,\mathrm{s}^{-1}$
propulsive force $f_\mathrm{p} = \mathrm{Pe}k_\mathrm{B}T/\sigma$	$0 - 2500\,k_BT/\mathrm{R}$	$0 - 0.65\,\mathrm{pN}$
LJ repulsion length $r_\mathrm{c}^\mathrm{p} = \sigma/2$	$0.03\,R$	$0.5\,\mu\mathrm{m}$
LJ potential depth ϵ	$10.5\,k_BT$	$4.4 \times 10^{-20}\,\mathrm{J}$

A set of simulation parameters for 2D vesicle systems in both model and physical units.